

BATTERIES

“Water-in-salt” electrolyte enables high-voltage aqueous lithium-ion chemistries

Liumin Suo,¹ Oleg Borodin,² Tao Gao,¹ Marco Olguin,² Janet Ho,² Xiulin Fan,¹ Chao Luo,¹ Chunsheng Wang,^{1*} Kang Xu^{2*}

Lithium-ion batteries raise safety, environmental, and cost concerns, which mostly arise from their nonaqueous electrolytes. The use of aqueous alternatives is limited by their narrow electrochemical stability window (1.23 volts), which sets an intrinsic limit on the practical voltage and energy output. We report a highly concentrated aqueous electrolyte whose window was expanded to ~3.0 volts with the formation of an electrode-electrolyte interphase. A full lithium-ion battery of 2.3 volts using such an aqueous electrolyte was demonstrated to cycle up to 1000 times, with nearly 100% coulombic efficiency at both low (0.15 coulomb) and high (4.5 coulombs) discharge and charge rates.

Lithium-ion (Li-ion) batteries power much of our digital and mobile lifestyle (1, 2). However, their adoption in more strategically important applications such as vehicle electrification and grid storage has been slower, mainly because of concerns raised over their safety, cost, and environmental impact (3). Most of these concerns come from the nonaqueous electrolytes needed to withstand the high voltages (>3.0 V) of the chemistries (4), because the ester-based solvents are highly flammable and reactive with the charged electrodes (5), and the lithium salt (LiPF₆) is thermally unstable and extremely toxic (6). Substantial costs are incurred not only directly by these electrolyte components but also to a larger degree by the stringent moisture-free process and safety management required for the dangerous combination of flammable electrolytes and energy-intensive electrodes (4, 7, 8).

Aqueous electrolytes could resolve these concerns (9–11), but their electrochemical stability window (1.23 V) is too narrow to support most of the electrochemical couples used in Li-ion batteries. Hydrogen evolution at the anode presents the most severe challenge, as it occurs at a potential (2.21 to 3.04 V versus Li, depending on pH value) far above where most Li-ion battery anode materials operate. Even in trace amounts, hydrogen severely deteriorates the electrode structure during cycling. A common practice to suppress hydrogen evolution in aqueous electrochemistry is to adjust the alkalinity (12, 13), so that the water reduction potential shifts downward to allow the use of anode materials otherwise prohibited under neutral or acidic conditions. However, as

the overall electrochemical stability window of aqueous electrolytes remains constant, anodic stability against oxygen evolution suffers a corresponding compromise, as illustrated by a Pourbaix diagram (9). A maximum voltage of 1.5 V was achieved in aqueous Li-ion batteries, where the residual currents for H₂ or O₂ evolution still brought high self-discharge rates despite the moderate cell voltage (9–11).

In contrast to nonaqueous electrolyte systems, where cathode and anode materials often operate far beyond the thermodynamic stability limits of electrolyte components (4, 14), kinetic protection from a solid-electrolyte interphase (SEI) in aqueous media has never been considered possible. Such interphases, situating between electrode surfaces and electrolyte, are formed by sacrificial electrolyte decomposition during the initial charging, and they constitute a barrier allowing ionic conduction but forbidding electronic conduction. Their presence substantially expands the usable electrochemical stability window of electrolytes. In conventional aqueous electrolytes, a protective interphase is absent because none of the decomposition products from water (H₂, O₂, or OH[−]) can deposit in a dense solid state. In the absence of interphases, aqueous Li-ion batteries are typically limited to low voltage (<1.5 V) and low energy density (<70 Wh/kg), often with rapid fading of capacity and low coulombic efficiency. The latter is especially pronounced at low C rates, where C refers to nominal capacity of the cell, and a rate of *n*C represents the discharge current that can drain this capacity in 1/*n* hours. (For most batteries, a rate of 1 C means that the discharge current will discharge the entire battery in 1 hour.)

We report the formation of such interphases in an aqueous electrolyte by manipulating the source of electrolyte decomposition during the initial charging processes. A “water-in-salt” electrolyte is obtained by dissolving lithium bis(trifluoromethane sulfonyl)imide (LiTFSI) at extremely high concentrations (molality >20 m)

in water. This leads to an anion-containing Li⁺ solvation sheath, which results in the formation of a dense interphase on the anode surface mainly arising from anion reduction. Combined with the substantially reduced electrochemical activity of water at such a high concentration, this highly concentrated water-in-salt electrolyte provides an expanded electrochemical stability window of ~3.0 V. A full aqueous Li-ion battery constructed with a model electrochemical couple (LiMn₂O₄ and Mo₆S₈) demonstrated an open circuit voltage (OCV) of 2.3 V and was cycled at nearly 100% coulombic efficiency for up to 1000 cycles at both low (0.15 C) and high (4.5 C) rates.

Water-in-salt electrolytes

LiTFSI was chosen as the salt because of its high solubility in water (>20 m at 25°C) and high stability against hydrolysis (15). When the LiTFSI concentration is above 5 m, the water-in-salt definition applies, as the salt outnumbers the solvent in this binary system by both weight and volume (fig. S1). In these solutions, the average number of water molecules available to solvate each ion is far below the “solvation numbers” that are well established in conventional electrolytes (~1.0 m). Instead, interionic attractions become more pronounced relative to solvent-ion interactions, incurring unusual physicochemical properties (16–20). More important, the interphasial chemistry on electrode surfaces could be altered as a direct consequence of the different cation solvation sheath structure (14, 21–24). This “cation solvation–interphase chemistry” correlation has been leveraged to manipulate the electrochemical behavior of nonaqueous electrolytes on both graphitic anode and metal oxide cathodes (17, 23, 25, 26), but its effect on aqueous electrolytes had remained unexplored. Figures S2 to S4 summarize the physical and transport properties of LiTFSI in water at varying concentrations. According to the thermal analysis of the highly concentrated solutions, solutions at both 20 and 21 m are “true” liquids at room temperature (25°C) that can be supercooled down to ~−90°C with negligible crystallinity (27). The room-temperature conductivity of 21 m solution remains ~10 mS/cm, comparable to that of nonaqueous electrolytes (9.0 mS/cm) used in commercial Li-ion batteries (figs. S3 and S4).

The electrochemical stability window for these aqueous electrolytes was evaluated with cyclic voltammetry (CV) on stainless steel electrodes, whose first cathodic and anodic scans are shown in Fig. 1. The overall stability window expands as the LiTFSI concentration increases, with both oxygen and hydrogen evolution potentials pushed well beyond the thermodynamic stability limits of water. Closer examination of Fig. 1A shows that the onset of reduction at all concentrations occurs at ~2.80 V, before rapidly accelerating at 2.63 V and then reaching a plateau. Quantum chemistry calculations predict the onset of LiTFSI reduction at such high concentrations around 2.7 to 2.9 V, which is slightly higher than the hydrogen evolution process (2.63 V) corresponding to the exponential current increase. Thus, prior

¹Department of Chemical and Biomolecular Engineering, University of Maryland, College Park, MD 20740, USA.

²Electrochemistry Branch, Sensor and Electron Devices Directorate, Power and Energy Division, U.S. Army Research Laboratory, Adelphi, MD 20783, USA.

*Corresponding author. E-mail: cswang@umd.edu (C.W.); conrad.k.xu.civ@mail.mil (K.X.)

to hydrogen evolution, the reduction of TFSI seems to result in a passivation process that intensifies with salt concentration and reduces the plateau current by more than an order of magnitude, from 2.47 mA/cm^2 (1 m) to 0.18 mA/cm^2 (21 m). This passivation eventually suppresses hydrogen evolution, pushing its onset from 2.63 V to 1.90 V. On the cathode side (Fig. 1B), oxygen evolution also seems to be suppressed with increasing salt concentration but no clear passivation process is observed, probably as a result of the reduced water activity when co-ordinated to Li^+ at high concentration as well as an inner Helmholtz layer increasingly populated by TFSI anions (28). Overall, a stability window of $\sim 3.0 \text{ V}$ is achieved because of the very high concentration of LiTFSI (Fig. 1C), with both cathodic ($\sim 1.9 \text{ V}$ versus Li) and anodic ($\sim 4.9 \text{ V}$ versus Li) limits beyond those defined by the Pourbaix diagram of water at pH 7 (cathodic $\sim 2.63 \text{ V}$ versus Li, anodic $\sim 3.86 \text{ V}$ versus Li).

The model cathode and anode materials LiMn_2O_4 and Mo_6S_8 (fig. S5) were chosen as active working electrodes in CV experiments to verify the expanded stability window. Figure 2A demonstrates two redox couples of LiMn_2O_4 , which gradually shift from 4.09/4.17 V and 4.22/4.31 V in 5 m solution to 4.17/4.37 V and 4.31/4.49 V in 21 m solution, while the reaction kinetics become slower at high salt concentrations. For Mo_6S_8 , a single lithiation/delithiation process was observed at ~ 2.5 V in dilute solutions, and only when salt concentrations reached 10 m or above did the second lithiation/delithiation at ~ 2.3 V appear. The modulation of redox processes

toward positive potentials, observed in all cases in Fig. 2A, is attributed to the Li^+ activity change in the solution according to the Nernst equation (see supplementary materials). It is this modulation that moves the second redox process of Mo_6S_8 into the expanded electrochemical stability window of the water-in-salt electrolyte, allowing the full and reversible use of its Li storage sites otherwise inaccessible in diluted aqueous solutions (fig. S6). Hence, a 2.3 V aqueous $\text{LiMn}_2\text{O}_4/\text{Mo}_6\text{S}_8$ full Li-ion cell is enabled by the water-in-salt electrolyte (Fig. 2B). In control electrolytes using LiNO_3 and Li_2SO_4 (figs. S7 and S8), similar positive modulations of Mo_6S_8 were observed; however, their limited solubility prohibited the appearance of the second lithiation/delithiation process. Even at the highest possible LiNO_3 concentration (12.5 m), hydrogen evolution still overwhelms the second lithiation of Mo_6S_8 at ~ 2.5 V versus Li (fig. S7), without any sign of passivation. Thus, the high concentration of LiTFSI in water not only reduces water activity and modulates redox potentials, but also suppresses hydrogen evolution through the formation of an interphase.

A high-voltage aqueous Li-ion battery

A full Li-ion cell using a LiMn_2O_4 cathode and a Mo_6S_8 anode was assembled to evaluate the viability of the water-in-salt electrolyte at 21 m (Fig. 2, B to D, and figs. S9 to S12). The cathode/anode mass ratio was set to 2:1 in order to compensate for the irreversible capacity at the Mo_6S_8 anode due to formation of SEI during the initial cycles. At 0.15 C, the cell displayed

two voltage plateaus at 1.50 V and 2.00 V, respectively (fig. S9), delivering a discharge capacity of 47 mAh per gram of total electrode mass. A conservative estimate made on the basis of average voltage and capacity places the energy density in the vicinity of 84 Wh per kilogram of total electrode mass. To further explore the energy density achievable in the ideal scenario where Li^+ consumption is minimized during the initial interphase formation, we matched a Mo_6S_8 anode recovered from a cycled full cell with a fresh LiMn_2O_4 cathode at 1:1 ratio. Such a full cell delivered an energy density of 100 Wh per kilogram of total electrode mass (fig. S11). A full aqueous Li-ion cell using Mo_6S_8 and $\text{LiNi}_{0.8}\text{Co}_{0.15}\text{Al}_{0.05}\text{O}_2$ cathode also cycled reversibly but yielded a lower capacity (fig. S13).

Figure 2, C and D, displays the cycling stability and coulombic efficiency of $\text{LiMn}_2\text{O}_4/\text{Mo}_6\text{S}_8$ full cells at low (0.15 C) and high (4.5 C) rates. Excellent stability with high capacity retention (68% with 1000 cycles at 4.5 C and 78% with 100 cycles at 0.15 C) and near 100% coulombic efficiency are observed at both rates (fig. S14). As shown by Dahn and colleagues, the most rigorous proof of stability does not come from the number of cycles, but rather from the time spent by a system at a fully charged state (29) as well as from high coulombic efficiency at low C rates. In previous studies, the cycling stability of aqueous Li-ion cells was often tactically evaluated at high instead of low rates, so that the effect of residual hydrogen and oxygen evolution on cycling stability would be less apparent. To reveal how much impact the trace parasitic

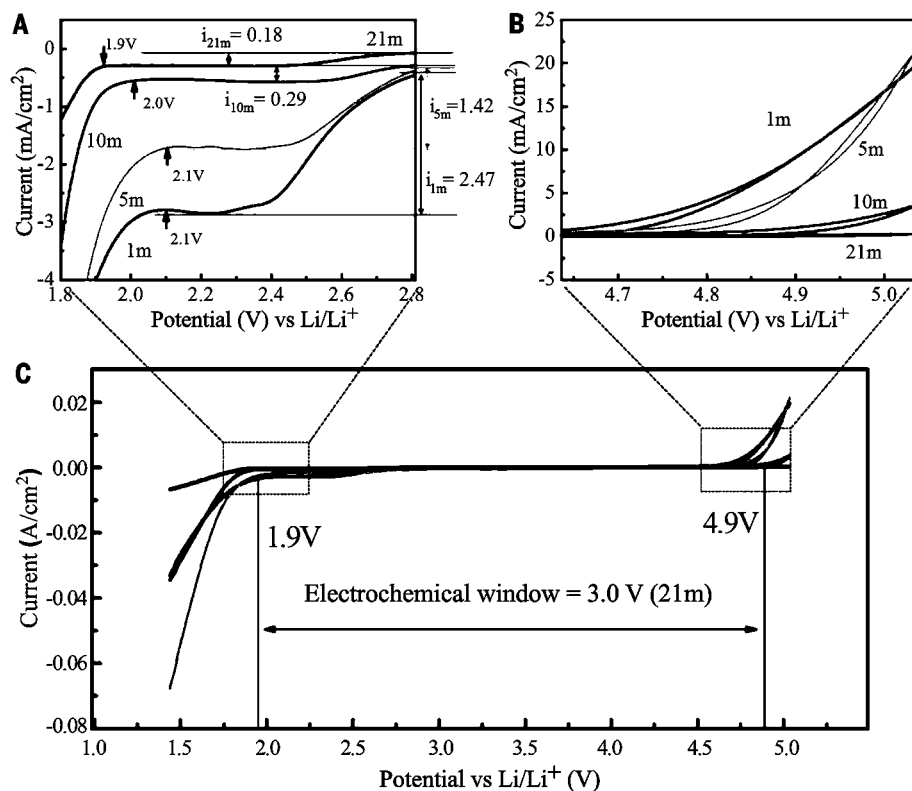


Fig. 1. The electrochemical stability window of LiTFSI-H₂O electrolytes on non-active electrodes. Measurements were taken at different concentrations (molality) with cyclic voltammetry (CV) on stainless steel working electrodes between -1.8 V and 1.8 V versus Ag/AgCl at 10 mV/s, wherein the potential has been converted to Li/Li⁺ reference for convenience. **(A)** Overall electrochemical stability window. **(B and C)** Magnified view of the regions outlined near anodic and cathodic extremes in (A).

reactions in water-in-salt electrolyte exert on full Li-ion cell performance, we monitored the open-circuit voltage decay of fully charged cells upon storage and then immediately measured the recoverable capacity. The results (figs. S15 and S16) confirm the negligible effect of either hydrogen or oxygen evolution. Only in longer-term cycling tests would the effect of parasitic reactions become more apparent, as evidenced by the slow but steady fading of capacity shown in Fig. 2, C and D; this finding suggests that the interphasial chemistry needs to be tailored for more effective protection. Elevated temperature (45°C) did not induce accelerated capacity fading, which indicates that the SEI formed should be stable against dissolution (fig. S12).

Interphasial chemistry and its importance

High salt concentration deviates solution dynamics from an ideal state (30). To quantify such deviation, we calculated the relative Li^+ activity coefficients in electrolytes based on the peak potential shifts as measured from CV (Fig. 2A). The details are given in supplementary text and tables S1 and S2; fig. S17 summarizes the dependence of these coefficients on salt concentration, which experiences a steady rise from 5 m to 21 m. According to Bockris and Reddy, this

increase of activity coefficients at high concentration reflects the deprived population of water as a free solvent and the intensified cation-anion interaction (30).

The interplay among Li^+ , TFSI⁻, and water was also investigated with spectroscopies. Major Raman vibrational signals are summarized in fig. S18 and table S3; Fig. 3A compares the shift of the most intense peak at 744 cm^{-1} as the salt concentration increases, with crystalline LiTFSI as the reference (top trace). Evidently this vibration mode is rather sensitive to the change of the anion environment, drifting from 744.6 cm^{-1} at 5.0 m to 748.5 cm^{-1} at 21 m. The latter is essentially identical to that in a crystalline lattice. On the basis of the previous assignment of a 748 cm^{-1} peak in nonaqueous electrolytes (37), we attribute this band to the formation of a percolated TFSI⁻ anionic network in the highly concentrated solutions. In the ^{17}O nuclear magnetic resonance (NMR) spectra, the two sets of oxygen nuclei were assigned to water (~0 ppm) and TFSI⁻ (~154 ppm), respectively; Fig. 3B displays the change in ^{17}O chemical shifts for both nuclei with LiTFSI concentration. The water ^{17}O signal is rather sensitive to the presence of salt, because Li^+ directly interacts with the lone pair electrons of water oxygen. Its coordination with Li^+ results in the deshielding, as indicated

by the downshift displacement in its chemical shift, while the increasing salt concentration above 10 m intensifies this effect. On the other hand, the ^{17}O signal at 154 ppm seems to be rather insensitive to the presence of salt, although its successive downshift is still visible. This can be attributed to the fact that oxygen on TFSI⁻ does not directly coordinate with Li^+ for salt concentrations less than 10 m.

Both oxygen nuclei display obvious peak broadening at salt concentrations greater than 10 m, as if the anion environment gradually transitions into a semisolid state similar to a LiTFSI crystal. Such an intimate interaction between cation and anion, as revealed by Raman and NMR spectroscopy, bears close resemblance to an ionic liquid, where on average each Li^+ is surrounded by at least one anion. Naturally, when Li^+ in this coordination environment is brought into the vicinity of the anode surface, TFSI⁻ would be reasonably expected to display its own electrochemical features.

The relationship between solution structure and electrochemical properties is further revealed from molecular dynamics simulations. For dilute solutions (≤ 5 m), Li^+ remains well hydrated in its primary solvation sheath with sufficient free water available (Fig. 3C). In such electrolytes, attempts to lithiate an anode, whose

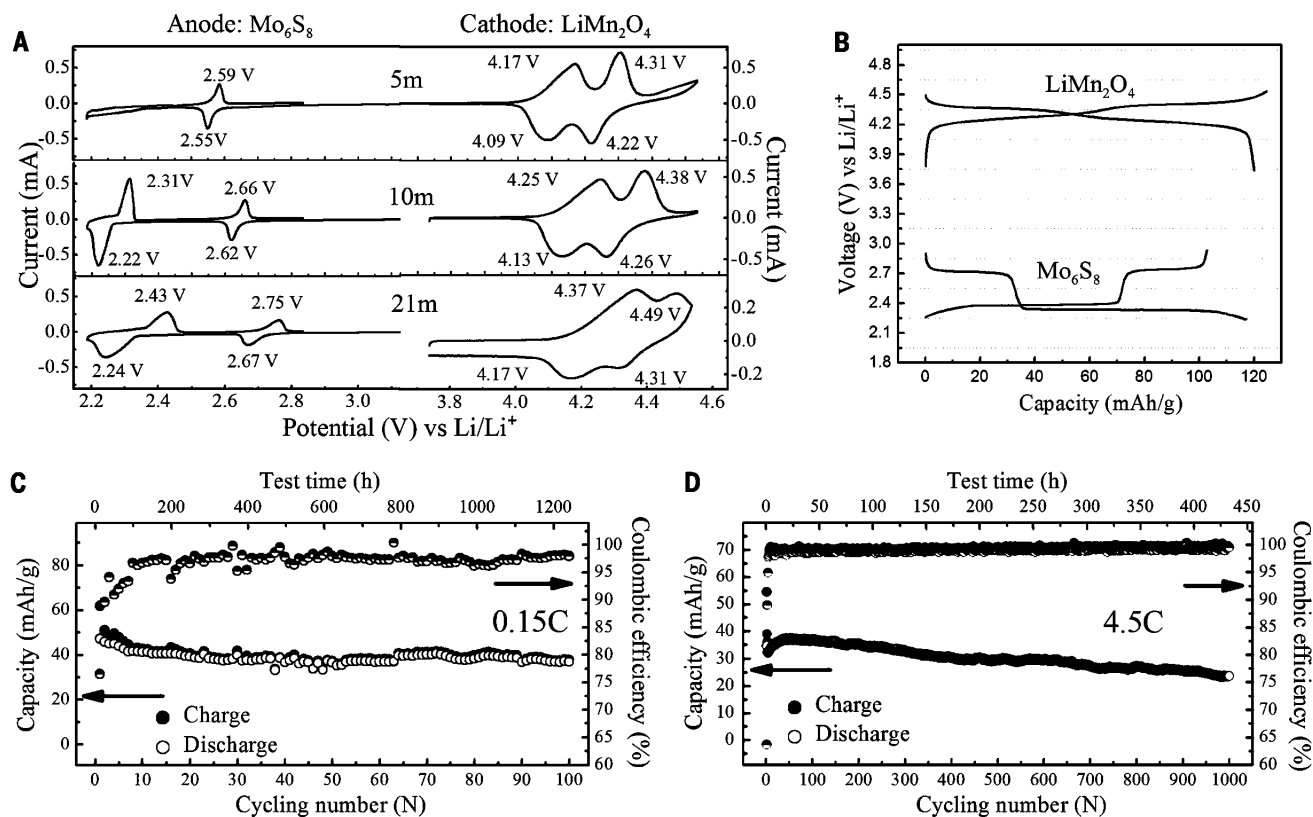


Fig. 2. Electrochemical performance on active electrodes. (A) Electrochemical stability window of electrolytes at various LiTFSI concentrations as measured with CV on active (LiMn₂O₄ and Mo₆S₈) electrode surfaces at 0.1 mV/s. (B) Typical voltage profile of LiMn₂O₄ and Mo₆S₈ electrodes in 21 m LiTFSI solution at constant current (0.2 C). Data in (A) and (B) were collected in a three-electrode device including Mo₆S₈ and LiMn₂O₄ as working electrodes and Ag/AgCl as reference electrode. (C and D) Cycling stability and coulombic efficiency of full aqueous Li-ion cells using Mo₆S₈ and LiMn₂O₄ as anode and cathode materials in 21 m LiTFSI solution, at low (0.15 C) and high (4.5 C) rates, respectively.

lithiation potential is below that of water reduction, would lead to preferential reduction of water and sustained hydrogen evolution, which would prevent not only any Li^+ intercalation but also any possible reduction of TFSI^- . However, with LiTFSI concentrations increased beyond 20 m, molecular dynamics simulation predicts that on average two TFSI^- anions would be observed in each Li^+ primary solvation sheath (Fig. 3D), and such a high probability of TFSI^- leads to an interphasial chemistry dominated by the reduction of TFSI^- .

The reduction potential of TFSI^- is also altered by its intimate interaction with Li^+ . According to density functional theory (DFT) calculations (Fig. 4A and fig. S19), aggregates such as $\text{Li}_2(\text{TFSI})(\text{H}_2\text{O})_x$ become reductively unstable below 2.9 V versus Li, which is substantially higher than the reduction potential for the isolated TFSI^- anion at 1.4 V (Fig. 4A) and hydrogen evolution at 2.63 V. Further corroborating the preferential reduction of TFSI^- over water, a density-of-states analysis obtained from DFT calculations indicates that both the TFSI^- conduction band minimum and the water valence band maximum shift to lower potentials with increasing salt concentration. At >20 m, this trend leads to a premature TFSI^- reduction and delayed water oxidation (Fig. 4B and supplementary materials). We therefore conclude that this reduction process generates sufficient LiF from TFSI^- to form an anode-

electrolyte interphase, which kinetically prevents sustained reduction of both water and TFSI^- in a similar manner as an SEI in nonaqueous electrolytes does. The earlier observation that TFSI^- was electrochemically reduced to LiF on an anode surface in nonaqueous electrolyte (32, 33) in conjunction with limited solubility of LiF in water make this speculation reasonable. In retrospect, an ideal lithium salt that could enable the formation of an aqueous SEI should be not only highly soluble and chemically stable in water but also susceptible to electrochemical reduction at a desired potential (i.e., a potential higher than that of H_2 evolution), producing a solid product insoluble in aqueous media. Lithium salts meeting these requirements include those based on fluoroalkyl sulfonylimide anions, to which LiTFSI belongs, as well as fluoroalkyl sulfonate anions. Compared with the higher cost of imides, sulfonates might make more appropriate candidates. At least one such sulfonate salt (lithium trifluoromethane sulfone) has been found to yield nearly identical electrochemical stability to that of LiTFSI (fig. S20).

To demonstrate the existence of an interphase in our aqueous electrolytes, we conducted x-ray photoelectron spectroscopy (XPS) on an anode recovered after a complete lithiation cycle. Figure 4C shows the valence electrons' binding energies for a few detected elements. Included as comparisons are the spectra of the pristine Mo_6S_8 , whose

$\text{Mo } 3d$ and $\text{S } 2p$ signals serve as references, and $\text{F } 1s$ detected therein at 689.5 eV came from poly(tetrafluoroethylene) (PTFE) used as binder in the composite electrode. The most conspicuous change after being charged to 2.3 V (corresponding to full lithiation of Mo_6S_8) is the disappearance of both $\text{S } 2p$ and $\text{Mo } 3d$ signals, and the appearance of $\text{Li } 1s$ and $\text{F } 1s$ signals, the latter of which is identified to be a CF_3 species. Hence, lithiation left the anode surface completely covered with species originated from TFSI^- , while the CF_3 species could arise from either excess LiTFSI remaining on the anode surface, or its incomplete reduction products. Etching this surface by Ar^+ reveals an underlying interphase consisting overwhelmingly of LiF , which not only precedes the reappearance of the original $\text{S } 2p$ and $\text{Mo } 3d$ signals but remains even after prolonged (1920 s) sputtering. This resistance against sputtering is undoubtedly the consequence of a very dense surface interphase.

On the basis of earlier reports that TFSI^- is electrochemically reduced to LiF (32, 33), we believe that in the current water-in-salt electrolytes, this LiF -rich interphase serves as an electron barrier preventing the reduction of water while allowing Li^+ migration. Evidence also comes from transmission electron microscopy (TEM) images of the cycled Mo_6S_8 , whose surface, when compared with the pristine state, is found to be covered with a crystalline phase 10 to 15 nm

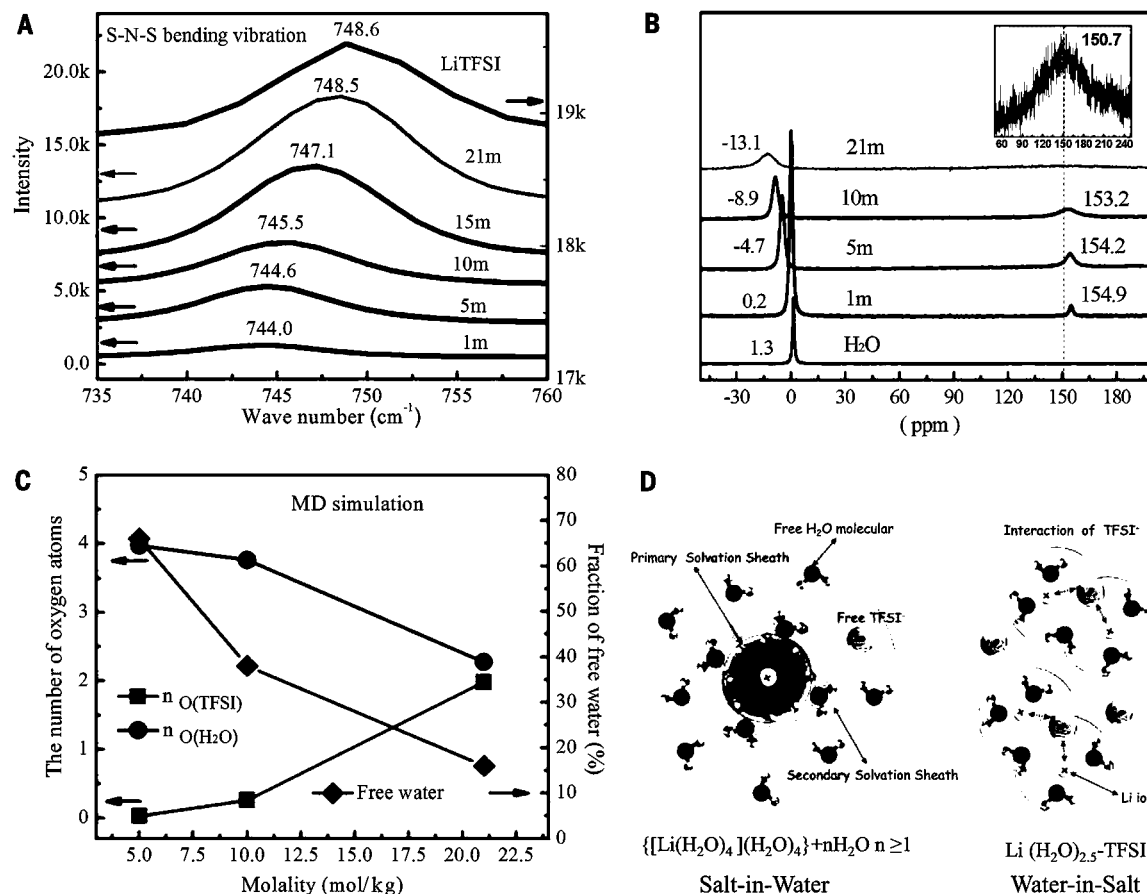


Fig. 3. The effect of LiTFSI concentration on ion-solvent and ion-ion interactions. (A) Progression of Raman vibration at $\sim 744 \text{ cm}^{-1}$ with salt concentration. (B) Change of chemical shifts for ^{17}O nuclei in solvent (water) and anion (TFSI^-). The inset shows the TFSI^- peak at 21 m. (C) Numbers of water and TFSI^- oxygen atoms within the Li^+ primary solvation sheath of 0.27 nm and the fraction of “free” water not bound to any Li^+ , all obtained from molecular dynamics simulations. (D) Illustration of the evolution of the Li^+ primary solvation sheath in diluted and water-in-salt solutions.

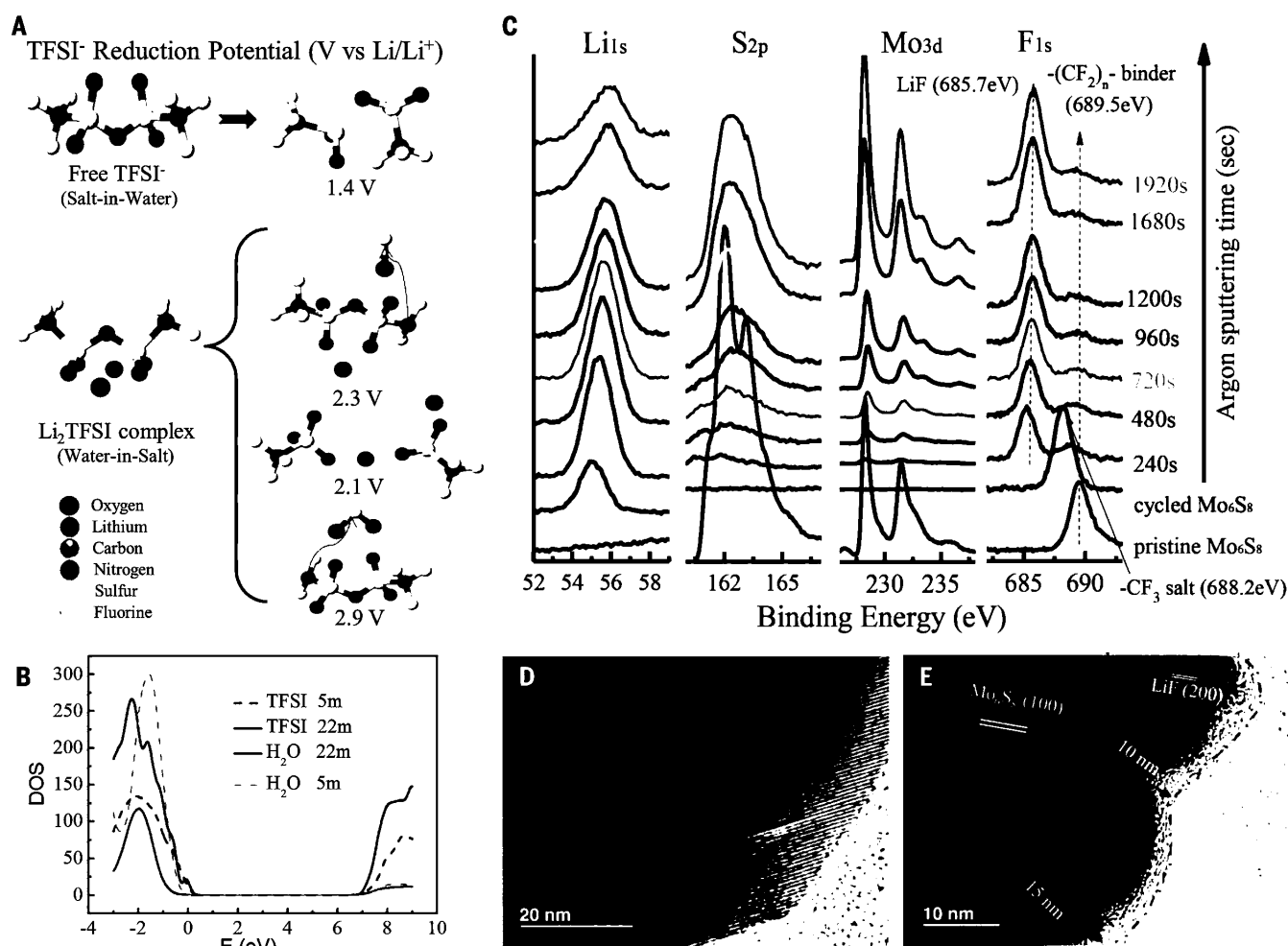


Fig. 4. SEI formation in aqueous electrolyte. (A) Predicted reduction potentials from G4MP2 quantum chemistry calculations. (B) Projected density of states (DOS) for H₂O-LiTFSI electrolyte from HSE06 DFT calculations. (C) X-ray photoelectron spectroscopy (XPS) spectrum of pristine (bottom) and cycled Mo₆S₈ at full lithiation state after various durations of Ar⁺ sputtering. (D and E) TEM images of pristine Mo₆S₈ (D) and cycled Mo₆S₈ (E).

thick (Fig. 4, D and E). The interplanar spacing of this crystalline phase identifies it as imperfect crystalline LiF. Further confirmation comes from TEM energy-dispersive x-ray spectroscopy (EDX) analysis (fig. S21), whose line scan reveals that F evenly distributes on the Mo₆S₈ particle surface. This aqueous LiF-based SEI, originating from TFSI⁻ reduction and crystalline in nature, seems to differ chemically from the composite interphases that have been well characterized in non-aqueous electrolytes (4, 14), where solvent reduction products contribute overwhelmingly as the chemical building blocks. On the cathode surface, however, no such LiF-based SEI was found even after extended cycling (figs. S22 and S23).

Summarizing all the spectra information, an overall picture of the Li⁺ solvation sheath and its role in interphasial chemistry emerges. In dilute solutions (< 5 m) (34, 35), the abundance of water can afford a conventional solvation sheath structure (i.e., four water molecules per Li⁺ in the primary and more in the loosely bound secondary sheath) (36), where Li⁺ and TFSI⁻ are well separated by water. When salt concentration increases to a certain level (>10 m), the

insufficient water population leads to a drastic change in Li⁺ solvation sheath structure. In particular, at 21 m, there are only 2.6 water molecules per Li⁺, which can no longer effectively neutralize the electrostatic field created by the formal charge on Li⁺; consequently, TFSI⁻ enters the Li⁺ solvation sheath, leading to intimate Li⁺-TFSI⁻ interactions as observed in Raman and ¹⁷O NMR spectroscopy. A direct result of this anion-containing solvation sheath is an interphasial chemistry on the anode consisting of mainly LiF from TFSI⁻ reduction, which is enabled not only by the high probability of TFSI⁻ in the Li⁺ solvation sheath, but also by its reduction potential, which is now higher than that of water. Simultaneously, the scarcity of free water molecules due to high salt concentration contributes to their inactivity that benefits both cathodic and anodic stability limits. These factors work in synergy to realize an expanded electrochemical stability window of 3.0 V (Fig. 1C).

Battery performance can be quantified with four parameters: cell voltage, capacity, coulombic efficiency, and cycling stability. The first two

determine the battery's energy density; the latter two dictate its lifetime and energy efficiency. For comparison, we plotted our water-in-salt battery in Fig. 5A against other aqueous systems previously investigated using these parameters. More than 1000 cycles were reported for electrochemical couples of LiMn₂O₄/acetylene black (37) and LiFePO₄/LiTi₂(PO₄)₃ (13). Their excellent stability, however, was achieved at the expense of voltage (<1.25 V) and energy density (<50 Wh/kg). On the other hand, efforts to increase cell voltage to ~1.50 V were accompanied by an appreciable compromise in cycling stability (10, 38–41). In all cases, energy densities were below 75 Wh/kg. The formation of an anode-electrolyte interphase in a water-in-salt electrolyte enables us to decouple voltage from cycling stability and achieve high values for both.

Note that the electrochemical couple used in our study (LiMn₂O₄ and Mo₆S₈) did not actually make full use of the expanded electrochemical stability window; thus, further advances in exploring more powerful and energetic battery chemistry for this electrolyte system are possible. From our perspective, perhaps more important

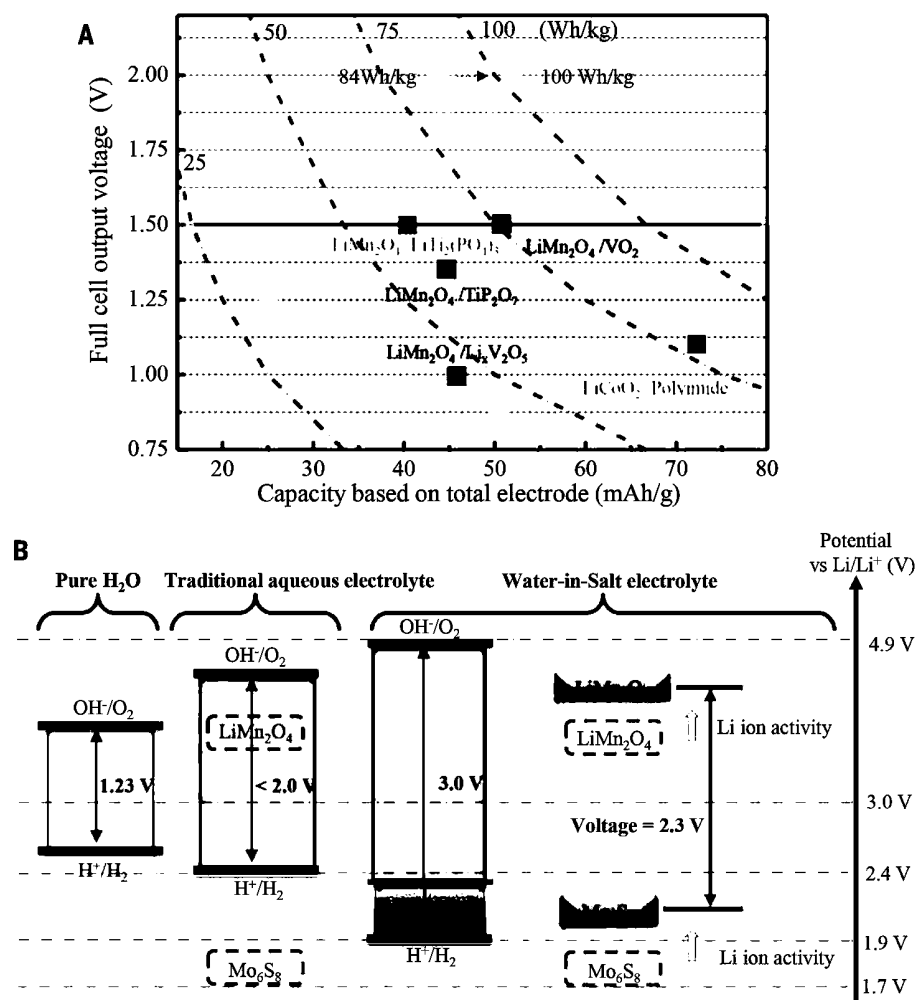


Fig. 5. The performance of aqueous Li-ion chemistries benefits from the expanded electrochemical stability window of aqueous electrolytes.

(A) Performance of aqueous Li-ion batteries based on various electrochemical couples. Color code for cycling stability: red, <100 cycles; blue, 100 to 200 cycles; green, >1000 cycles. (B) Illustration of expanded electrochemical stability window for water-in-salt electrolytes together with the modulated redox couples of LiMn₂O₄ cathode and Mo₆S₈ anode caused by high salt concentration.

than the electrochemical performance described in Fig. 2, C and D, is the fact that an interphase could form and function in aqueous electrolytes, which opens new avenues to aqueous electrochemistry (Fig. 5B).

REFERENCES AND NOTES

- M. Armand, J. M. Tarascon, *Nature* **451**, 652–657 (2008).
- M. S. Whittingham, *Chem. Rev.* **104**, 4271–4302 (2004).
- B. Dunn, H. Kamath, J. M. Tarascon, *Science* **334**, 928–935 (2011).
- K. Xu, *Chem. Rev.* **104**, 4303–4418 (2004).
- L. Hu, K. Xu, *Proc. Natl. Acad. Sci. U.S.A.* **111**, 3205–3206 (2014).
- A. Hammami, N. Raymond, M. Armand, *Nature* **424**, 635–636 (2003).
- J. B. Goodenough, Y. Kim, *Chem. Mater.* **22**, 587–603 (2010).
- J. M. Tarascon, M. Armand, *Nature* **414**, 359–367 (2001).
- H. Kim et al., *Chem. Rev.* **114**, 11788–11827 (2014).
- W. Li, J. R. Dahn, D. S. Wainwright, *Science* **264**, 1115–1118 (1994).
- Y. G. Wang, J. Yi, Y. Y. Xia, *Adv. Energy Mater.* **2**, 830–840 (2012).
- W. Li, W. R. McKinnon, J. R. Dahn, *J. Electrochem. Soc.* **141**, 2310–2316 (1994).
- J.-Y. Luo, W.-J. Cui, P. He, Y.-Y. Xia, *Nat. Chem.* **2**, 760–765 (2010).
- K. Xu, *Chem. Rev.* **114**, 11503–11618 (2014).
- S. F. Lux et al., *J. Electrochem. Soc.* **160**, A1694–A1700 (2013).
- C. A. Angell, C. Liu, E. Sanchez, *Nature* **362**, 137–139 (1993).
- K. Yoshida, M. Tsuchiya, N. Tachikawa, K. Dokko, M. Watanabe, *J. Phys. Chem. C* **115**, 18384–18394 (2011).
- L. Suo, Y.-S. Hu, H. Li, M. Armand, L. Chen, *Nat. Commun.* **4**, 1481 (2013).
- K. Ueno et al., *J. Phys. Chem. B* **116**, 11323–11331 (2012).
- J.-W. Park et al., *J. Phys. Chem. C* **117**, 4431–4440 (2013).
- K. Xu, Y. Lam, S. S. Zhang, T. R. Jow, T. B. Curtis, *J. Phys. Chem. C* **111**, 7411–7421 (2007).
- K. Xu, A. von Cresce, *J. Mater. Chem.* **21**, 9849–9864 (2011).
- M. Nie et al., *J. Phys. Chem. C* **117**, 25381–25389 (2013).
- S.-K. Jeong et al., *Electrochem. Commun.* **31**, 24–27 (2013).
- Y. Yamada et al., *J. Am. Chem. Soc.* **136**, 5039–5046 (2014).
- K. Yoshida et al., *J. Am. Chem. Soc.* **133**, 13121–13129 (2011).
- G. Perron, D. Brouillette, J. E. Desnoyers, *Can. J. Chem.* **75**, 1608–1614 (1997).
- D. W. McOwen et al., *Energy Environ. Sci.* **7**, 416–426 (2014).
- J. C. Burns et al., *J. Electrochem. Soc.* **158**, A255 (2011).
- J. O. M. Bockris, A. K. N. Reddy, *Modern Electrochemistry* (Kluwer Academic/Plenum, New York, ed. 2, 2000).
- D. M. Seo, O. Borodin, S.-D. Han, P. D. Boyle, W. A. Henderson, *J. Electrochem. Soc.* **159**, A1489–A1500 (2012).
- E. Krämer et al., *J. Electrochem. Soc.* **160**, A356–A360 (2013).
- A. v. Cresce, S. M. Russell, D. R. Baker, K. J. Gaskell, K. Xu, *Nano Lett.* **14**, 1405–1412 (2014).
- Y. Marcus, *Chem. Rev.* **109**, 1346–1370 (2009).
- H. Ohtaki, T. Radnai, *Chem. Rev.* **93**, 1157–1204 (1993).
- G. Bogle, R. Vazquez, S. Greenbaum, A. Cresce, K. Xu, *J. Phys. Chem. Lett.* **4**, 1664–1668 (2013).
- Y.-G. Wang, Y.-Y. Xia, *J. Electrochem. Soc.* **153**, A450–A454 (2006).
- J. Y. Luo, Y. Y. Xia, *Adv. Funct. Mater.* **17**, 3877–3884 (2007).
- H. Wang, Y. Zeng, K. Huang, S. Liu, L. Chen, *Electrochim. Acta* **52**, 5102–5107 (2007).
- H. Wang, K. Huang, Y. Zeng, S. Yang, L. Chen, *Electrochim. Acta* **52**, 3280–3285 (2007).
- H. Qin, Z. P. Song, H. Zhan, Y. H. Zhou, *J. Power Sources* **249**, 367–372 (2014).

ACKNOWLEDGMENTS

C.W. and K.X. gratefully acknowledge both funding and inspiration from P. Liu of DOE ARPA-E (DEAR0000389). We also acknowledge the support of the Maryland Nano Center and its Nisplab. The Nisplab is supported in part by the NSF as a MRSEC Shared Experimental Facility. We thank K. Gaskell, Y.-F. Lam, S.-C. Liou, A. Goyal, and S. R. Raghavan for technical support and helpful discussions. Modeling efforts were supported by ARL Enterprise for Multiscale Research of Materials. M.O. was supported by an Oak Ridge Associated Universities postdoctoral fellowship.

SUPPLEMENTARY MATERIALS

www.sciencemag.org/content/350/6263/938/suppl/DC1
Materials and Methods
Supplementary Text
Figs. S1 to S27
Tables S1 to S5
References (42–61)

19 March 2015; accepted 25 September 2015
10.1126/science.aab1595

This copy is for your personal, non-commercial use only.

If you wish to distribute this article to others, you can order high-quality copies for your colleagues, clients, or customers by [clicking here](#).

Permission to republish or repurpose articles or portions of articles can be obtained by following the guidelines [here](#).

The following resources related to this article are available online at www.sciencemag.org (this information is current as of November 19, 2015):

Updated information and services, including high-resolution figures, can be found in the online version of this article at:

<http://www.sciencemag.org/content/350/6263/938.full.html>

Supporting Online Material can be found at:

<http://www.sciencemag.org/content/suppl/2015/11/18/350.6263.938.DC1.html>

A list of selected additional articles on the Science Web sites **related to this article** can be found at:

<http://www.sciencemag.org/content/350/6263/938.full.html#related>

This article **cites 60 articles**, 10 of which can be accessed free:

<http://www.sciencemag.org/content/350/6263/938.full.html#ref-list-1>

This article has been **cited by** 1 articles hosted by HighWire Press; see:

<http://www.sciencemag.org/content/350/6263/938.full.html#related-urls>

This article appears in the following **subject collections**:

Chemistry

<http://www.sciencemag.org/cgi/collection/chemistry>

Physics

<http://www.sciencemag.org/cgi/collection/physics>